SANDIA REPORT
SAND2022-0942
Unclassified Unlimited Release
Printed January 2022

Mesoscale simulations of pressure-shear loading of granular tungsten carbide

Brian J. Demaske

Prepared by
Sandia National Laboratories
Albuquerque, New Mexico
87185 and Livermore,
California 94550

Issued by Sandia National Laboratories, operated for the United States Department of Energy by National Technology & Engineering Solutions of Sandia, LLC.

ABSTRACT

Numerical simulations of pressure-shear loading of a granular material are performed using the shock physics code CTH. A simple mesoscale model for the granular material is used that consists of a randomly packed arrangement of solid circular or spherical grains of uniform size separated by vacuum. The grain material is described by a simple shock equation of state, elastic perfectly plastic strength model, and fracture model with baseline parameters for WC taken from previous mesoscale modeling work. Simulations using the baseline material parameters are performed at the same initial conditions of pressure-shear experiments on dry WC powders. Except for some localized flow regions appearing in simulations with an approximate treatment of sliding interfaces among grains, the samples respond elastically during shear, which is in contrast to experimental observations. By extending the simulations to higher shear wave amplitudes, macroscopic shear failure of the simulated samples is observed with the shear strength increasing with increasing stress confinement. The shear strength is also found to be strongly dependent on the grain interface treatment and on the fracture stress of the grains, though the variation in shear strength due to fracture stress decreases with increasing stress confinement. At partial compactions, the transverse velocity histories show strain-hardening behavior followed by formation of a shear interface that extends through the transverse dimensions of the sample. Near full compaction, no strain hardening is observed and, instead, the sample transitions sharply from an elastic response to formation of an internal shear interface. Agreement with experiment is shown to worsen with increasing confinement stress with simulations overpredicting the shear strengths measured in experiment. The source of the disagreement can be ultimately attributed to the Eulerian nature of the simulations, which do not treat contact and fracture realistically.

ACKNOWLEDGEMENTS

I would like to thank Jeff LaJeunesse (Org. 5417) for providing a starting point for the CTH simulations, answering questions related to pressure-shear testing, and providing his feedback and advice throughout the course of this work. I would also like to thank Tracy Vogler (Org. 8363) for helpful discussion as this work was progressing and Travis Voorhees (Org. 8363) for providing feedback on this report.

CONTENTS

LIST OF FIGURES

LIST OF TABLES

This page left blank

ACRONYMS AND DEFINITIONS

Abbreviation	Definition
AMR	adaptive mesh refinement
CTH	a 3D Eulerian hydrocode developed at Sandia National Laboratories
EOS	equation of state
LAMMPS	a molecular dynamics code developed at Sandia National Laboratories
MD	molecular dynamics
MPD	maximum packing density
PDV	Photon Doppler velocimetry
SEM	scanning electron microscopy

1. INTRODUCTION

Granular ceramic materials are common in nature and have important applications in planetary science, i.e., terrestrial impact events [1, 2], and in the performance of modern armor systems [3], where the failed region ahead of the penetrator is thought to be in a granular or comminuted state [4, 5]. As such, it is important to understand how these materials fail at high strain rates. Normal plate impact experiments, in which a projectile with a flat nose is launched at high velocities into a flat, stationary target, have been used to characterize the dynamic compaction response of granular ceramic materials [6-13]. However, because of their 1D nature, these types of experiments do not provide information about shear stresses in the target, which are needed for developing constitutive models. The pressure-shear (or oblique plate impact) experiment [14] was developed as a modification of the normal plate impact experiment, where the projectile nose and target are both inclined at an angle with respect to the projectile velocity. The target itself is comprised of a thin layer of sample material sandwiched between two high-strength anvils. Provided that there is no slip at the interface, the impact between the angled projectile nose and target generates both normal and shear waves that propagate into the target. Velocity measurements of the rear surface of the target can be used to determine the dynamic shear strength of the thin sample layer. Because of their difficulty, only a few such tests have been carried out on granular ceramic materials, including sand (SiO_2) [15], tungsten carbide (WC) [16], alumina (Al_2O_3) [17], and boron carbide (B_4C) [18].

Many processes contribute to the macroscopic failure behavior of granular materials, including elastic-plastic deformation and damage or fracture of grains, intergranular contact and friction, removal of porosity due to compaction, and localized melting at grain surfaces. To further the understanding of dynamic compaction in powders, mesoscale models of granular materials have been used in hydrocodes to simulate normal plate impact tests for several decades. Initially these studies focused on metal powders [19-23] (or metal-matrix composites [24]), where the shock response was shown to be dominated by ductile flow at low amplitudes and melting, jet formation, and turbulent flow at high amplitudes. Several years later, the same methodology was applied to study the shock compaction of ceramic powders [25-30]. Despite the brittle nature of these materials, simulation predictions were shown to agree well with the experimental shock Hugoniot and shock wave rise time data in the form of a similar power-law exponent in Hugoniot stress versus strain rate. Parametric studies assessed the effect of micro- and macro-scale properties of the mesoscale powder model on the compaction response up to full densification and found that the response was most sensitive to the microscopic yield and fracture strength of the grains, the number of dimensions in the simulation, the initial porosity of the powder, and the approximate method used to treat intergranular contact [28, 30].

Despite the success of mesoscale simulations in predicting the dynamic compaction response of ceramic powders, little work has been done to test whether these types of simulations could also be used to model the dynamic shear strength. To our knowledge, only a single study by LaJeunesse has attempted to examine this question [15]. In that work, LaJeunesse performed 3D mesoscale simulations in conjunction with pressure-shear experiments on sand to provide insight into how the shear strain history of the sample was affected by the target geometry and impact velocity. LaJeunesse observed increased shear strain accumulation in simulations where the target geometry was such that the shear wave arrived prior to the sample being fully loaded by the normal wave. In addition, he found that the rise time of the shear wave decreased with increasing impact velocity. Simulations in which grains were allowed to slide by one another showed an increase in compaction and greater shear strain accumulation compared to simulations where grains were welded together upon first contact, which is the default behavior in hydrocodes. In contrast to the granular samples in experiment, which could not support the full amplitude of the incident shear waves and showed evidence of grain fracture in post-shot scanning electron microscopy (SEM) images, the mesoscale powder model in the 3D hydrocode simulations did not exhibit conclusive evidence of failing macroscopically under shear. Simulations with the default welded grain behavior followed the maximum normal and shear stress state set by the choice of anvil materials and impact conditions, while simulations with the approximate treatment of intergranular sliding were only slightly below this limit.

This work expands upon the mesoscale simulations in Ref. [15] focusing on granular WC instead of sand as there is additional data from pressure-shear experiments [16] against which to compare simulation results. In addition to a full 3D geometry for the simulations, a 2D geometry is also considered, which is motivated by the success of previous 2D mesoscale simulations in predicting the normal shock compaction response of granular WC [27, 28]. The WC grains are treated using the same material models used in previous mesoscale simulations. Using the baseline material parameter sets for WC, both 2D and 3D simulations do not show evidence of macroscopic failure under the same initial conditions as in experiment, which is in agreement with previous mesoscale simulations on sand. To probe the shear failure surface of the mesoscale powder model, simulations are extended to much higher shear wave amplitudes, which are outside of the range possible in experiment. Parametric studies varying the interface treatment and fracture stress of the grains are performed to examine the effects on the normal and shear response. In general, simulations tend to overpredict the dynamic shear strength of WC powder compared to experiment with the magnitude of the overprediction increasing with increasing confinement stress. This overprediction is attributed to an inadequate treatment of grain contact and fracture in the current computational model and signals the need for more sophisticated fracture or damage models in future hydrocode simulations or alternate numerical methods better equipped to handle contact and fracture.

2. SIMULATION DETAILS

2.1. Computational model of a pressure-shear test

Mesoscale simulations of pressure-shear testing of granular WC are carried out using the multi-material shock physics code CTH [31]. The computational model follows from previous mesoscale simulations of pressure-shear testing of sand [15] with some geometry modifications to allow for direct comparison with pressure-shear experiments on granular WC [16]. Only a rectangular core of the full cylindrical flyer-target system is included in the simulation domain, which is illustrated in Figure 1 for both 2D and 3D geometries. Components in the model include the flyer nose, front and rear anvils, and granular WC layer. The interface between the flyer and front anvil is perfectly flat. At time zero, the flyer is given an initial velocity of $u_0 = V\cos\theta$ along the x-axis and a velocity of $v_0 = V\sin\theta$ along the y-axis, where V and θ are the magnitude of the initial velocity and angle of inclination of the flyer and target with respect to the impact direction, respectively. The impact generates normal and shear waves that propagate into the flyer and front anvil. Boundaries along the x-axis are free, while periodic boundaries are maintained in the transverse dimensions. Small vacuum regions (1-mm-thick) on flyer and rear anvil free surfaces are included to allow for expansion of material during release. The anvil thicknesses are 8 mm to coincide with experiment, while the flyer thickness is set to 12 mm to prevent release from the flyer free surface at the granular WC layer prior to release from the rear anvil free surface. The flyer and anvil thicknesses in the illustrations are greatly reduced from the actual values in the simulations to reduce the aspect ratio and thereby aid in visualization of the granular WC layer.

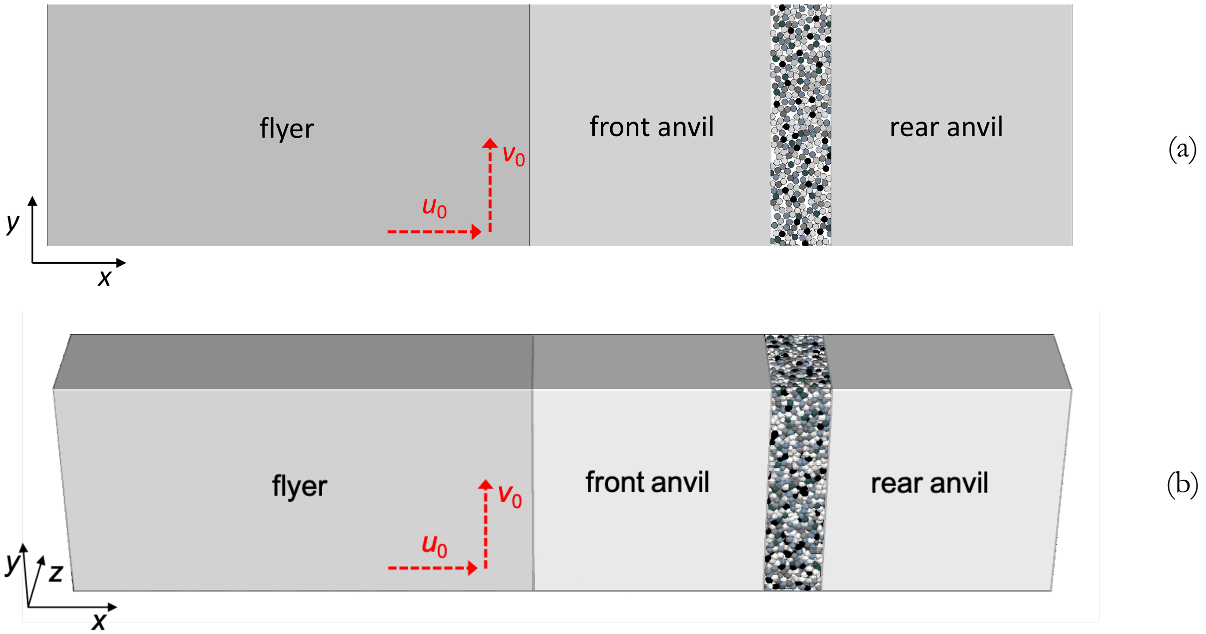

Figure 1. Illustration of the simulation geometry in (a) 2D and (b) 3D. The thicknesses of the flyer and anvils are greatly reduced to aid in visualization of the powder sample, which is modeled as a randomly packed assembly of circular/spherical grains separated by vacuum.

The granular WC layer is modeled as a collection of randomly packed grains, which are represented as circles in 2D and spheres in 3D. Grain realizations are generated using the granular package of the molecular dynamics (MD) code LAMMPS [32]. For the initialization step, each grain is treated as a finite-sized circular or spherical particle that interacts elastically with other particles in a periodic box. The thickness of the box along the x-axis is 0.25 mm to match the experimental sample thickness, while the box cross-section is 1 mm and 0.5×0.25 mm for the 2D and 3D geometries, respectively. The cross-section of the 3D box corresponds to 20×10 grain diameters in agreement with previous mesoscale simulations on sand. All particles have a diameter of 25 μm, which lies within the range of WC grain sizes in experiment (=20-32 μm). As a first step, the box is randomly seeded with particles. Initial densities of the samples in experiment were not measured, so we assume an initial sample porosity of 35%, which is the same as used in previous pressure-shear simulations on sand. This gives a total of 332 and 2483 particles in the 2D and 3D geometries, respectively. The insertion step does not account for the finite size of the particles, so a step-size-limited MD run is performed after the insertion step to reduce the amount of particle overlap. Once the particle overlap is sufficiently reduced, all particles are given a small randomly-oriented velocity and a constant-energy MD run is performed for the time it takes for an average particle to travel several mean free path lengths. The final particle positions from the 2D and 3D MD simulations are used to build up the initial mesoscale powder models in the CTH simulations.

The flyer and anvil materials are inserted first into the CTH mesh followed by the WC grains. The order of the material insertion is important as CTH works on a first-in basis, which means only grain material that does not overlap with the anvils is inserted into the mesh, while remaining material is omitted. Regions of the mesh that do not contain inserted material are treated as vacuum. The flyer and anvils, which are composed of Ti-6Al-4V in experiment, are described by a Mie-Grüneisen equation of state (EOS) and an elastic perfectly plastic strength model. The bulk sound speed c_0, initial density ρ_0, and Poisson ratio ν are chosen to ensure simulations give the same longitudinal and transverse sound speeds as measured in experiment [33]. The condition of elastic anvils is enforced by design in the experiments. To simplify the computational model, the anvils are forced to remain elastic by setting the yield stress of the Ti-6Al-4V strength model to an arbitrarily large value. The WC grains are treated using a Mie-Grüneisen EOS and an elastic perfectly plastic strength model with a cap on the tensile pressure to model fracture. The choice of a simple strength model for WC follows from previous mesoscale simulations on the shock compaction of granular WC [27, 28, 30]. Parameter values for the material models are given in Table 1.

Table 1. Parameters for materials used in the CTH simulations. The yield stress for Ti-6Al-4V is set to an arbitrarily large value to suppress yielding, while fracture of Ti-6Al-4V is not modeled. Parameters for WC are taken from Ref. [27].

Parameter	WC	Ti-6Al-4V
Initial density, ρ_0 (g cm^{-3})	15.56	4.415
Bulk sound speed, c_0 (km s^{-1})	5.26	4.91
Hugoniot slope, S	1.15	1.028
Gruneisen parameter, Γ	1.0	1.23
Specific heat, C_V (J kg^{-1} K^{-1})	172	521
Yield stress, Y_0 (GPa)	5	-
Poisson ratio, ν	0.2	0.317
Fracture stress, σ_f (GPa)	4	-

In Eulerian codes like CTH, interfaces between different materials are not modeled explicitly. Instead, special consideration is given to cells containing multiple materials. By default, all materials that reside in a single cell share a common velocity. This type of treatment leads to a welded or stiction behavior at interfaces between two or more materials. An alternate treatment is to set the shear velocity gradients in these cells to zero, which leads to sliding at interfaces between two or more materials. Previous mesoscale simulations on sand [15] and WC [30] have shown that the way mixed-material cells are treated, either using the default welded behavior or by enforcing the slide condition, has a strong effect on simulation results. Both treatments are employed for the simulations presented in this work and results are compared to see which leads to better agreement with experiment. All grains are described by a common material model for WC. Therefore, to distinguish neighboring grains and allow for the enforcement of the slide condition, any grains that come in contact should have different material identification numbers (IDs). CTH limits the number of materials allowed in each simulation, so all grains cannot be assigned unique material IDs. Fortunately, through the course of a simulation, a given grain will interact with only a small number of grains in its local neighborhood. Only those nearby grains must have unique material IDs, while the IDs of the remaining grains are inconsequential. Thus, for a given central grain, all grains within a radius R = 50 μm, i.e., twice the grain diameter, are assigned unique material IDs, as shown schematically in Figure 2. This value is chosen to allow for a fair amount of relative motion among the grains before a grain encounters another grain with the same material ID. However, further investigation is necessary to ensure that R is large enough such that the number of such encounters is small enough as to not noticeably affect the simulation results.

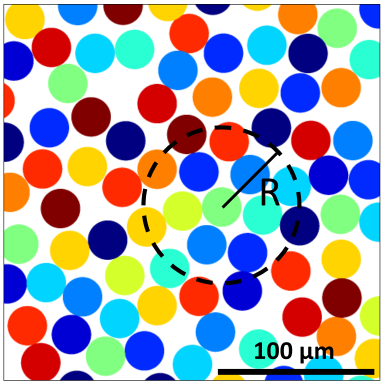

Figure 2. Section of the 2D mesoscale powder model with grains colored according to their material identification number (ID). All grains with centers lying within a radius R = 50 μm about a given central grain are assigned unique material IDs (colors in the figure).

The flyer and anvil materials are the same, so the impact is symmetric and particle velocities on either side of the interface are given by $u = u_0/2$ and $v = v_0/2$. In experiment, Photon Doppler velocimetry (PDV) probes are used to record the normal and transverse velocity histories at the rear of the target. To mimic this type of measurement in the simulations, we follow the approach in Ref. [15] and place lines (in 2D) or planes (in 3D) of Lagrangian tracer particles at the anvil-sample interfaces and at the rear anvil free surface. The average positions and velocities of the interfaces can then be computed by averaging the positions and velocities of the individual tracers. The instantaneous average position of the front anvil-sample interface along the x-axis is denoted by x_f and the corresponding velocity component is denoted by $\dot{x}_f$. The subscripts *r* and *fs* denote the rear anvil-sample interface and rear anvil free surface, respectively. For the anvil-sample interfaces, the tracers can be placed directly at the interface. However, for the rear anvil free surface, doing so leads to high frequency oscillations in the transverse velocity. By shifting the position of the tracer particles into the rear anvil away from the free surface by the width of a computational cell, such oscillations can be removed completely. The average normal σ and shear τ stresses, normal ϵ and shear γ strain, and normal $\dot{\epsilon}$ and shear $\dot{\gamma}$ strain rates are given by

$$\sigma = \frac{1}{2}\rho_A c_{L,A}\dot{x}_{fs}, \qquad \epsilon = 1 - \frac{x_r - x_f}{h_0}, \qquad \dot{\epsilon} = \frac{\dot{x}_f - \dot{x}_r}{h_0}, \tag{1}$$

$$\tau = \frac{1}{2}\rho_A c_{S,A}\dot{y}_{fs}, \qquad \gamma = \frac{y_f - y_r}{h}, \qquad \dot{\gamma} = \frac{\dot{y}_f - \dot{y}_r}{h}, \tag{2}$$

where ρ_A, $c_{L,A}$, and $c_{S,A}$ are the density, longitudinal sound speed, and transverse sound speed of the rear anvil. The expressions for stress assume that the anvil materials remain elastic during the measurement time window, which is always true in the simulations. The instantaneous sample thickness $h = x_r - x_f$ is used in the expression for the shear strain rate and h_0 denotes the sample thickness at $t = 0$.

2.2. Adaptive mesh refinement

To accurately resolve the wave motion in the powder, the computational mesh must be several times smaller than the grain size. Following from previous mesoscale simulations on sand, the current simulations use a mesh resolution of 12 cells/grain, which corresponds to a computational cell size of ~2 μm for the assumed WC grain size of 25 μm. Uniformly meshing the 3D geometry with a mesh resolution of 2 μm and a transverse size of 0.5×0.25 mm would result in a simulation domain of 473 million cells (ignoring boundary cells). In such a large calculation, most of the computational resources would be wasted computing high-fidelity wave motion in the flyer and anvils, which occupy an overwhelming majority of the simulation domain. The granular WC sample occupies only a thin slice of the domain – 0.25 mm out of 30 mm total thickness. Therefore, instead of a uniform meshing scheme, an adaptive mesh refinement (AMR) scheme is adopted in order to preferentially place high-resolution mesh in regions of the simulation domain where it is needed, while allocating a much coarser mesh to all other regions. For the 2D geometry, where uniform meshing leads to a manageable number of cells (~8 million), the AMR scheme is not strictly necessary, but greatly reduces the required computational cost.

At a high level, the AMR scheme in CTH works by dividing the simulation domain into non-overlapping blocks with each block divided into $N_X \times N_Y \times N_Z$ computational cells. The user defines the number of blocks along each dimension B_X, B_Y, B_Z at the lowest refinement level (level 0). Then, during the simulation, the code evaluates indicators to determine if a given block should be refined or unrefined subject to the condition that neighboring blocks can differ by a maximum of one refinement level (2:1 isotropic refinement). The mesh resolution along the x-axis at a given refinement level n is given by

$$d_X = \frac{x_2 - x_1}{2^n N_X B_X}, \tag{3}$$

where x_1 and x_2 denote the lower and upper boundaries of the simulation domain. The mesh resolutions along the other directions d_Y and d_Z (3D only) are defined similarly. The AMR parameters are determined by fixing the mesh resolution at the highest refinement level at ~2 μm and keeping the cell aspect ratio as close as possible to unity. This leads to a total of 5 and 3 refinement levels for the 2D and 3D simulations, respectively. The cell dimensions for each refinement level are given in Table 2. The slightly larger cell dimension along the x-axis for the 3D geometry compared to the y and z directions is a result of requiring an even number of cell divisions N_X and a whole number of level-0 blocks B_X.

Table 2. Cell dimensions at each refinement level for 2D (left) and 3D (right) AMR simulations.

Level	d_x (μm)	d_y (μm)
0	62.50	62.50
1	31.25	31.25
2	15.63	15.63
3	7.81	7.81
4	3.91	3.91
5	1.95	1.95

Level	d_x (μm)	d_y (μm)	d_z (μm)
0	15.66	15.63	15.63
1	7.83	7.81	7.81
2	3.91	3.91	3.91
3	1.96	1.95	1.95

Refinement indicators are defined that satisfy the following requirements: (1) WC grains and anvil-sample and anvil-vacuum interfaces should be resolved at the highest refinement level, (2) remaining bulk regions in the sample and anvils should be resolved at the minimum refinement level that does not noticeably affect the simulated quantity of interest, which for our purposes are the motions of the anvil-sample interfaces and rear anvil free surface, and (3) vacuum regions should be resolved at the lowest refinement level. To determine the necessary mesh resolution to satisfy (2), 2D mesoscale simulations are performed varying the refinement level from 0 (lowest level) to 4 (second highest level). Rear surface velocity histories from the AMR simulations are plotted in Figure 3 along with those from a uniform mesh simulation with a mesh resolution equal to the resolution at the maximum refinement level in the AMR scheme. Normal velocity is largely unaffected by refinement level, while the transverse velocity shows oscillations for the lowest few refinement levels that do not appear in the uniform mesh calculation. As the refinement level is increased, the oscillations dampen, and the velocity converges upon the uniform mesh result. At a refinement level of 3, which corresponds to cell dimensions of 7.81×7.81 μm, there is almost no difference between the AMR and uniform mesh results. Thus, we fix the refinement level in the bulk of the flyer and anvil materials at 3 for the 2D simulations and 1 for the 3D simulations. In addition, because it takes a finite time for the first normal wave to reach the sample, the activation of the AMR indicators that force maximum refinement in the sample and relevant interfaces is delayed until the wave arrives at the sample. This saves some computational resources at the beginning of a simulation and has no effect on the simulation results.

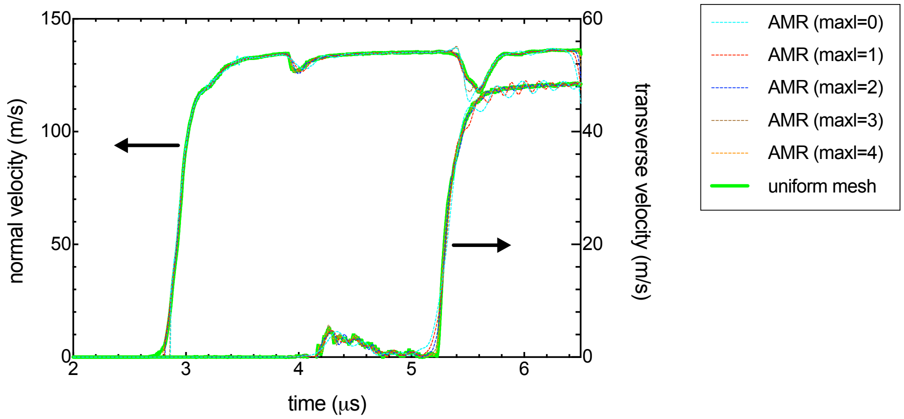

Figure 3. Rear surface velocity history for 2D AMR simulations for different refinement levels in the bulk of the flyer and anvils. A uniform mesh simulation with a resolution equal to the highest refinement level (level 5) is shown for comparison.

A view of the blocks for the region surrounding the granular WC sample is shown in Figure 4 for a 2D AMR simulation. The sample is refined at the maximum refinement level of 5, and the bulk of the anvils is at a refinement level of 3. Between these regions are small transition regions with a refinement level of 4, which are required to maintain the 2:1 isotropic refinement condition. Although the AMR blocks have a rectangular shape, the computational cells themselves are approximately squares, which is accomplished by setting $N_X = 22$ and $N_Y = 8$. Similar parameters are also used in the 3D geometry to maintain approximately cubic cells. The AMR indicators are defined using material IDs, so the high-resolution mesh moves with the sample during a simulation. This is also true for the rear anvil free surface (not shown in the figure). To assess the performance of the AMR scheme, AMR and uniform mesh simulations are performed, where the resolution of the uniform mesh corresponds to the maximum refinement level in the AMR scheme. We find that for the 2D geometry the AMR simulation is ~8× faster than the uniform mesh simulation, for an identical number of processors. Similarly, AMR is ~5× faster for the 3D geometry.

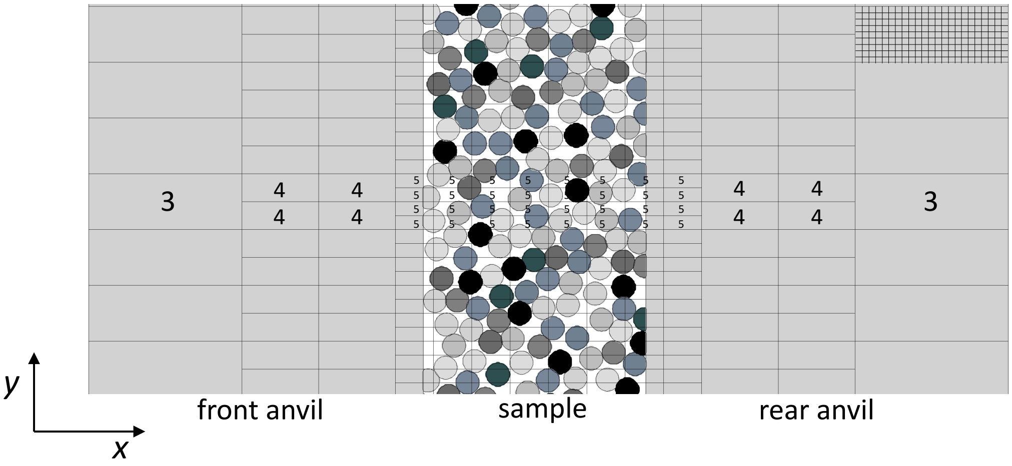

Figure 4. Region near the powder sample from a 2D simulation with the AMR meshing scheme. The overlaid lines show the AMR block structure with representative blocks labeled with their respective refinement level. Note: AMR blocks are rectangular, while the actual computational cells are square. See upper right AMR block in the figure, which illustrates the division of an AMR block into computational cells.

3. SIMULATION RESULTS

3.1. Direct comparison with pressure-shear experiments on granular WC

Simulations of pressure-shear loading of granular WC are carried out using the computational model developed in the previous section. Both 2D and 3D geometries are considered as well as two types of treatments for mixed-material cells containing WC grains: the default welded treatment and an approximate treatment of intergranular sliding using the slide algorithm in CTH. See Sec 2.1 for more details on how the slide condition is enforced in the mesoscale powder model. For simplicity, simulations with the default welded treatment are referred to as stiction simulations, while those with intergranular sliding are referred to as slide simulations. The nose angle θ is $20°$ for all three shots, and the impact velocity V is set to 66, 121, or 145 m/s to reproduce the impact conditions of pressure-shear experiments on granular WC [16]. The termination time for the simulations is chosen as 7 μs, which corresponds to the approximate time it takes for any shear waves originating at the granular WC layer to reach the rear anvil free surface prior to unloading of the normal compressive stress state. The much larger radial dimensions of the flyer and target in experiment compared to the axial thicknesses justifies the use of the simplified rectangular model in the simulations as radial release waves can be safely ignored up to the end of the measurement time window.

2D stiction and slide simulations and 3D stiction simulations reach the specified termination time, while 3D slide simulations stall at ~1.3 μs, which corresponds to the arrival time of the normal wave at the granular WC layer. The time step in these simulations is found to drop rapidly due to several cells within the granular WC layer exhibiting very high sound speeds (>22 km/s) as well as the presence of small, high-velocity (>5 km/s) fragments in nearly empty cells adjacent to cells with high volume fractions of WC. The cells with high sound speeds are found to contain very small volume fractions ($<10^{-10}$) of WC, which are in unphysical states of tension (-27 GPa) and temperature (>250,000 K). Discard sets based on temperature, pressure, and sound speed are added to remove material in these unphysical states, while discard sets based on cell volume fraction and velocity are added to remove the small, high-velocity fragments. With these discard sets included, the simulations maintain reasonable sound speeds and velocities through to the desired termination time. Over the course of a single run, enforcement of the discard sets leads to ~1.6% of the WC grain material being removed from the simulation. It is assumed the removal of such a small amount of material does not produce a noticeable effect on the simulation results, though it may be difficult to check this assumption as simulations without the discard sets are unable to be run past the point when the initial normal wave arrives at the sample.

Velocity histories from the rear anvil free surface are shown in Figure 5(a) for the current set of mesoscale simulations along with PDV measurements from experiment. Time is shifted such that the zero corresponds to the arrival of the normal wave at the rear surface. The shear wave arrives at the rear surface ~2.3 μs after the normal wave. The expected normal and transverse velocities are given by $u_0 = V\cos\theta$ and $v_0 = V\sin\theta$, respectively. Two dips appear in the simulated normal velocity histories at ~1.2 μs and ~2.6 μs. The first dip is caused by a disturbance in the normal velocity from the shear wave arriving at the granular WC layer, while the second dip is caused by the normal release wave originating from the rear anvil free surface reflecting at the interface with the granular WC layer. The second dip is absent from the normal velocity history for the 3D slide simulation at $V = 66$ m/s, which shows an increase in velocity instead. The source of this difference in behavior compared to the other simulations is not known definitively at this time but is probably related to the relatively low normal velocity level after rise also observed for this simulation and is discussed further in the next paragraph. Experiments at $V = 121$ and 145 m/s exhibit similar, though less pronounced, dips in the normal velocity near the times observed in the simulations. No such dips in normal velocity are evident for the experiment at $V = 66$ m/s.

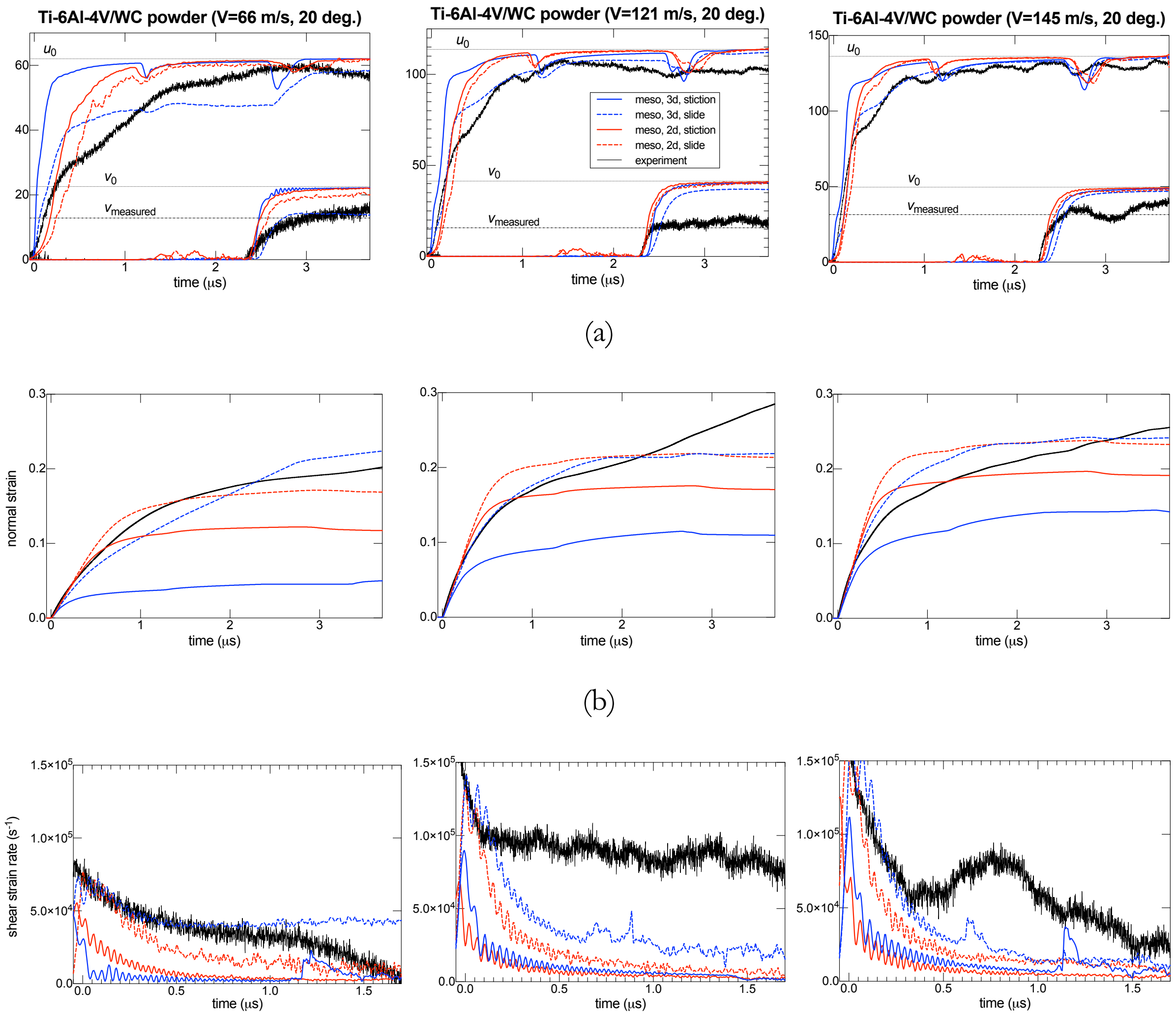

(a)

(b)

(c)

Figure 5. Comparison of mesoscale simulations with pressure-shear experiments [16] on granular WC: (a) normal and transverse rear surface velocities, (b) normal strain, and (c) shear strain rate starting from the shear wave rise.

Corresponding simulated and experimental normal strain histories are shown in Figure 5(b). The normal strain histories for the simulations are calculated using Eq. (1). Experiments do not have access to the positions/velocities of the anvil-sample interfaces, so the rear surface normal velocity history $\dot{x}_{fs}$ is used to compute the normal strain rate via $\dot{\varepsilon} = (u_0 - \dot{x}_{fs})/h_0$, where h_0 is the initial sample thickness. The strain rate is then numerically integrated to get the normal strain history ε. The above expression is only strictly true when the sample is in a homogeneous normal stress state. However, 3D simulations show that normal strains calculated directly from the sample-anvil interfaces and indirectly from the rear free surface normal velocity history are both very similar, so it is expected this is also the case in experiment. In general, simulated samples tend to compact rapidly during the initial part of the normal wave rise then reach a plateau in the normal strain history with very little compaction observed at later times. By contrast, experiments show a much more gradual compaction response with significant normal strain accumulation at later times. The exception is the 3D slide simulation at $V = 66$ m/s in which the normal strain increases nearly linearly after the initial rise. The simulated normal velocity rises rapidly then remains at a nearly constant level $< u_0$ for ~2 μs and afterwards jumps up to near u_0, whereas the normal velocity rise in experiment is more gradual and does not exhibit this two-level behavior. Some thoughts on the origin of the unusual behavior in the low-velocity 3D slide simulation include numerical issues with the slide algorithm at low velocities, loss of momentum due to removal of grain material via the discard sets, or an issue with the AMR indicators, but more work is necessary to understand it in detail.

Comparing the 2D and 3D simulations, the 2D simulations reach higher normal strains after the initial part of the normal wave rise. This difference in the compaction behavior is a result of differences in the grain packing in 2D versus 3D. Previous mesoscale modeling work looking at compaction shock waves in granular WC found that the transition in compaction mechanisms from rigid grain rearrangement to grain deformation occurred at a packing density of ~73% for random 2D arrangements of uniformly sized circular grains [27]. No transition in compaction mechanisms has been estimated for random 3D arrangements of uniformly sized spheres. However, the limiting density of random packings of hard spheres is estimated to be 63.7% [34]. In this work, the initial packing density of the simulated powder samples is ~65%, so samples in the 2D simulations can compact at least partially through rigid grain rearrangement. By contrast, the initial packing density is above the limiting density for random packings of hard spheres, so it is reasonable to assume that grains in the undeformed 3D powder model are already in a jammed or locked arrangement. Any compaction of the powder sample in the 3D simulations must therefore be accompanied by grain deformation. This difference makes the 3D model stiffer, at least initially, than the 2D model, which leads to less compaction during the initial part of the normal wave rise.

The 3D slide and 2D stiction simulations exhibit a similar normal velocity response up to ~0.3 μs, at which point the 2D stiction simulations show a rapid rise to u_0, while the 3D slide simulations show a more gradual rise that is more representative of experiment. The similar behavior during the initial normal wave rise agrees with results of previous mesoscale simulations of single compaction shocks through granular WC, which found 2D stiction and 3D slide simulations to exhibit nearly the same shock Hugoniot for similar initial states [30]. In the pressure-shear configuration, the normal stress wave reverberates within the sample many times until reaching the final compressive stress state. Thus, for the 3D slide simulations, there is additional compaction of the granular WC layer with each successive reverberation, while further compaction is limited for the 2D stiction simulations. Such behavior can be seen clearly in the normal strain history response. This behavior makes sense as grains in the 2D stiction simulations become welded together at contact points formed by the initial normal wave, whereas grains can slide over one another in the 3D slide simulations, thus allowing the sample to compact further with each successive wave reverberation.

The arrival time of the shear wave is predicted well by the simulations, which is expected as the bulk sound speed c_0 and elastic properties of Ti-6Al-4V were matched to experiment. Transverse velocity histories from experiment do not reach v_0, which indicates that the sample is unable to support the shear stress transmitted by the front anvil. The shear flow stress measured in experiment is proportional via Eqn. (2) to the measured transverse velocity level v_{measured}, which is indicated in Figure 5(a) for each of the three shots. Both 2D and 3D stiction simulations show the transverse velocity to reach v_0 indicating that the mesoscale powder model is not failing and is able to transmit nearly the full amplitude of the shear wave from the front anvil to the rear anvil. Visual inspection of the simulated powder sample during and after loading by the shear wave shows that there is some grain deformation and movement during the shear wave rise, but afterward the grains reach a stable configuration in which no further shear flow is visible. Enforcing the slide condition for the grains leads to a somewhat reduced transverse velocity level relative to the stiction simulations, which becomes more pronounced as the impact velocity is decreased. The reduction in transverse velocity is also more pronounced in 3D than in 2D, and out of all the simulations the 3D slide simulation at $V = 66$ m/s exhibits the lowest transverse velocity relative to the expected level. However, even in that case, the sample remains largely intact and does not show visible signs of macroscopic shear flow. Simulations with grain sliding enforced do show some localized flow in the granular WC layer, see snapshots in Figure 6, which is exacerbated at low impact velocities. It is hypothesized that the diminished transverse velocity levels for the slide simulations, as shown in Figure 5(a), can be attributed to these localized flow regions. The localized flow is also more pronounced in 3D than in 2D, which is reflected in the relative differences in the steady transverse velocity levels.

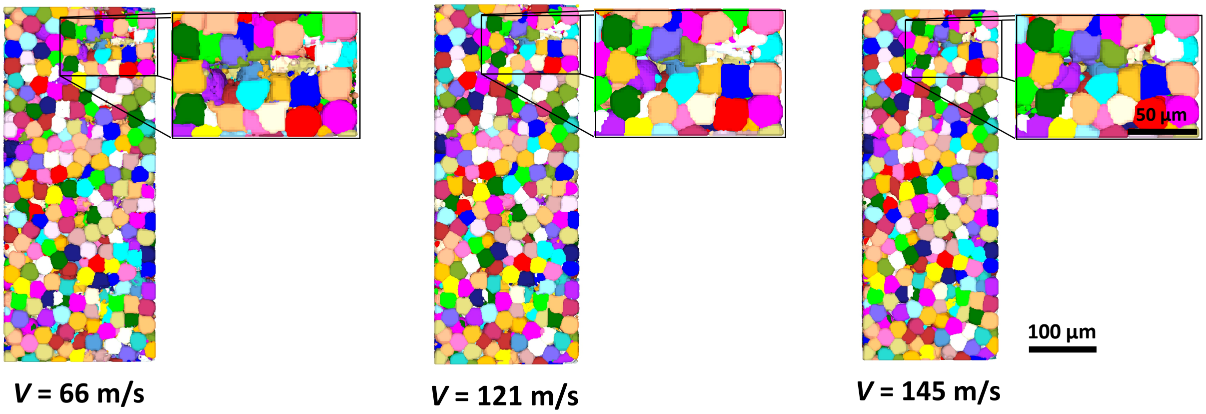

Figure 6. Snapshots of the granular WC layer from 3D simulations at *t* = 3.5 µs. A region exhibiting localized flow is shown zoomed in for each snapshot. The localized flow becomes more pronounced as the impact velocity is lowered.

The shear strain rate history is shown in Figure 5(c) starting at $t = 2.3$ µs, which corresponds to just before the shear wave rise. Experiments do not have access to the positions/velocities of the anvil-sample interfaces, so the rear surface transverse velocity history $\dot{y}_{fs}$ is used to compute the shear strain rate via $\dot{\gamma} = (v_0 - \dot{y}_{fs})/h_0$, where h_0 is the initial sample thickness. Like the expression for the normal strain rate, the above expression is only strictly true when the sample is in a homogeneous state of shear stress. Moreover, the above expression leads to an underprediction of the actual shear strain rate as it uses the initial sample thickness h_0 instead of the instantaneous sample thickness h. Experiments show a plateau to a non-zero shear strain rate following the shear wave rise. By contrast, simulations with the grain stiction behavior show much lower shear strain rates, close to zero, indicating very little shear strain (given by the area under the shear strain rate curve) in the sample compared to experiment. Simulations with grain sliding behavior show higher shear strain rates relative to the simulations with the grain stiction behavior, which is in agreement with previous mesoscale simulations of pressure-shear loading of sand [15]. In addition, the differences between the shear strain rates for the two types of interface treatments are larger in 3D than in 2D. The higher shear strains found in the slide simulations are thought to be due to the localized flow behavior occurring within the sample, as discussed in the previous paragraph, and are not indicative of any macroscopic shear failure of the simulated powder model.

3.2. Probing the failure surface of the mesoscale powder model

Simulation results presented in the previous section showed that the mesoscale model for the granular WC layer did not exhibit macroscopic shear failure under the same impact conditions as in experiment. Although simulations with the slide condition enforced among the WC grains exhibit a steady transverse velocity level that is below v_0, visual inspection of the granular sample after the shear wave rise shows that it remains in a stable configuration with only localized flow regions, see Figure 6. Simulations with grain stiction behavior reach v_0 with the samples showing no signs of macroscopic shear failure or localized flow regions. To probe the shear failure surface of the mesoscale powder model, simulations are performed in which the transverse velocity of the impactor is varied, while the normal velocity is held fixed. In this way, the amplitude of the initial shear wave can be varied, while keeping the amplitude of the normal wave fixed. Given normal and shear wave amplitudes σ_{el} and τ_{el}, the impact velocity V and nose angle θ are given by

$$V = \frac{2\sigma_{el}}{\rho_A c_{L,A}} \left[1 + \left(\frac{c_{L,A}\tau_{el}}{c_{S,A}\sigma_{el}} \right)^2 \right]^{1/2} \tag{4}$$

$$\theta = \tan^{-1}\left(\frac{c_{L,A}\tau_{el}}{c_{S,A}\sigma_{el}} \right), \tag{5}$$

where ρ_A, $c_{L,A}$, and $c_{S,A}$ are the initial density, longitudinal sound speed, and transverse sound speed of the impactor and anvil materials. To remain consistent with the previous simulations, the flyer and anvil materials are kept as Ti-6Al-4V. As the yield stress is essentially infinite in the model for Ti-6Al-4V, yielding of the anvil materials is suppressed independent of the impact parameters. Though not physically realistic, this simplifies the simulations as Eqs. 1 and 2 will hold for all simulations presented in this section.

The shots in experiment were carried out at $\theta = 20^{\circ}$ and $V = 66$, 121, and 145 m/s, which correspond (via Eqs. (1) and (2)) to normal wave amplitudes $\sigma_{el} = 0.838$, 1.537, and 1.842 GPa and shear wave amplitudes $\tau_{el} = 0.158$, 0.290, and 0.347 GPa, respectively. For the first set of simulations, σ_{el} is fixed at 0.838 GPa and simulations are performed increasing τ_{el} from 0.1 to 2 GPa. Rear surface transverse velocity histories for these runs are shown in Figure 7 for the 2D geometry. Both stiction and slide simulations at $\tau_{el} = 0.1$ GPa reach the expected transverse velocity level, which is consistent with results presented in the previous section. Upon increasing τ_{el} beyond 0.1 GPa, the transverse velocity levels continue to increase in the stiction simulations and approach the expected level. At $\tau_{el} = 2$ GPa, the observed quasi-steady level after rise is significantly less than the expected level. During the shear loading, the individual grains in the sample show significant deformation and join to form clusters leaving behind void regions that grow over time as the clusters increase in size. A snapshot showing the deformation of the granular WC layer for a 2D stiction simulation at $\tau_{el} = 2$ GPa is shown in Figure 7. Very different behavior is observed in the slide simulations as τ_{el} is increased beyond 0.1 GPa. For $\tau_{el} > 0.5$ GPa, further increases to τ_{el} does not lead to an increase in the transmitted transverse velocity level. On average, the upper bound in transverse velocity increases over time. Visual inspection of the sample during loading by the shear wave shows significant shear flow as grains deform and slide over one another. For the 2D slide simulation at $\tau_{el} = 2$ GPa, the transverse velocity obtains a maximum near $t = 6.2$ μs then decreases. The start of the decrease coincides with the formation of a line-like shear interface within the sample. Once the internal shear interface spans the transverse size of the sample, see simulation snapshot in Figure 7, the transverse velocity starts to drop as all shearing motion becomes concentrated at this interface.

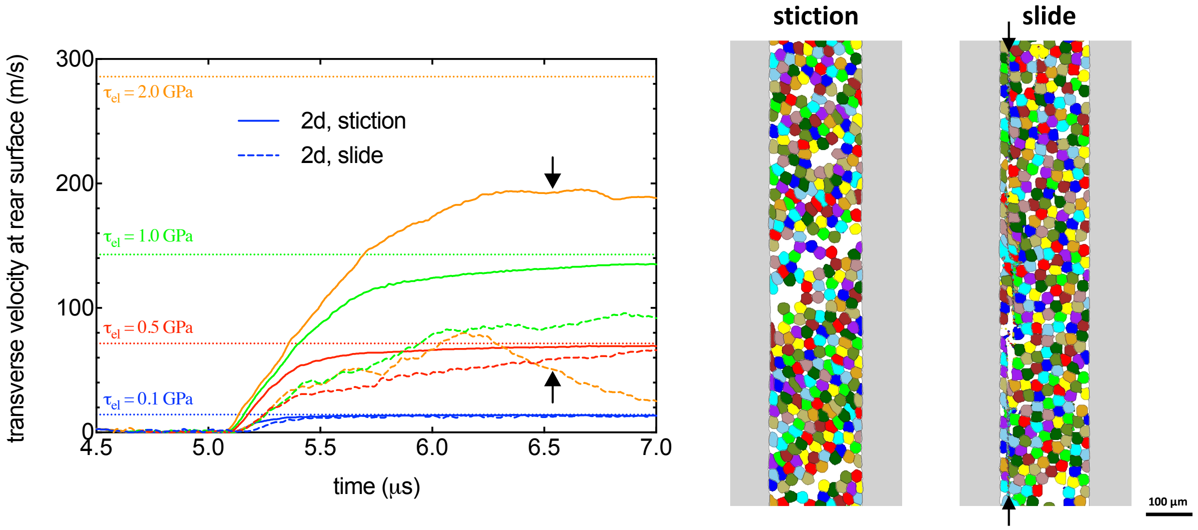

Figure 7. Transverse velocity history from 2D simulations at a fixed normal wave amplitude σ_{el} of 0.838 GPa and shear wave amplitudes τ_{el} of 0.1, 0.5, 1, and 2 GPa. Expected transverse velocity levels for each shear wave amplitude are denoted by horizontal dotted lines. Snapshots of the WC grains at the time indicated in the plot are shown for both slide and stiction simulations.

Additional simulations, like the ones presented in the previous paragraph, are carried out for different values of σ_{el} to determine the shear strength of the mesoscale powder model as a function of the confinement stress. Normal wave amplitudes σ_{el} of 1.842 and 4 GPa are chosen, where the value of 1.842 GPa corresponds to the normal wave amplitude of the experiment at $V = 145$ m/s and the value of 4 GPa is equal to the fracture stress (=4 GPa) and close to the yield strength (=5 GPa) used in the baseline model parameters for WC. The normal wave amplitude corresponding to the experiment at $V = 121$ m/s is not considered as it is only ~17% less than that for the 145 m/s experiment. Only simulations with grain sliding behavior are considered as the transverse velocity levels that can be supported by simulations with grain stiction behavior are many times greater than observed in experiment. For example, at $\sigma_{el} = 0.838$ GPa, the rear surface transverse velocity about 1 μs after shear wave rise is ~14 m/s in experiment, whereas the 2D mesoscale powder model with grain stiction behavior can support transverse velocities up to ~200 m/s, see the solid orange curve in Figure 7. For each value of σ_{el}, simulations are carried out progressively increasing the shear wave amplitude τ_{el} from 1 GPa up to a maximum of 2 GPa in steps of 0.25 GPa. Both 2D and 3D geometries are considered.

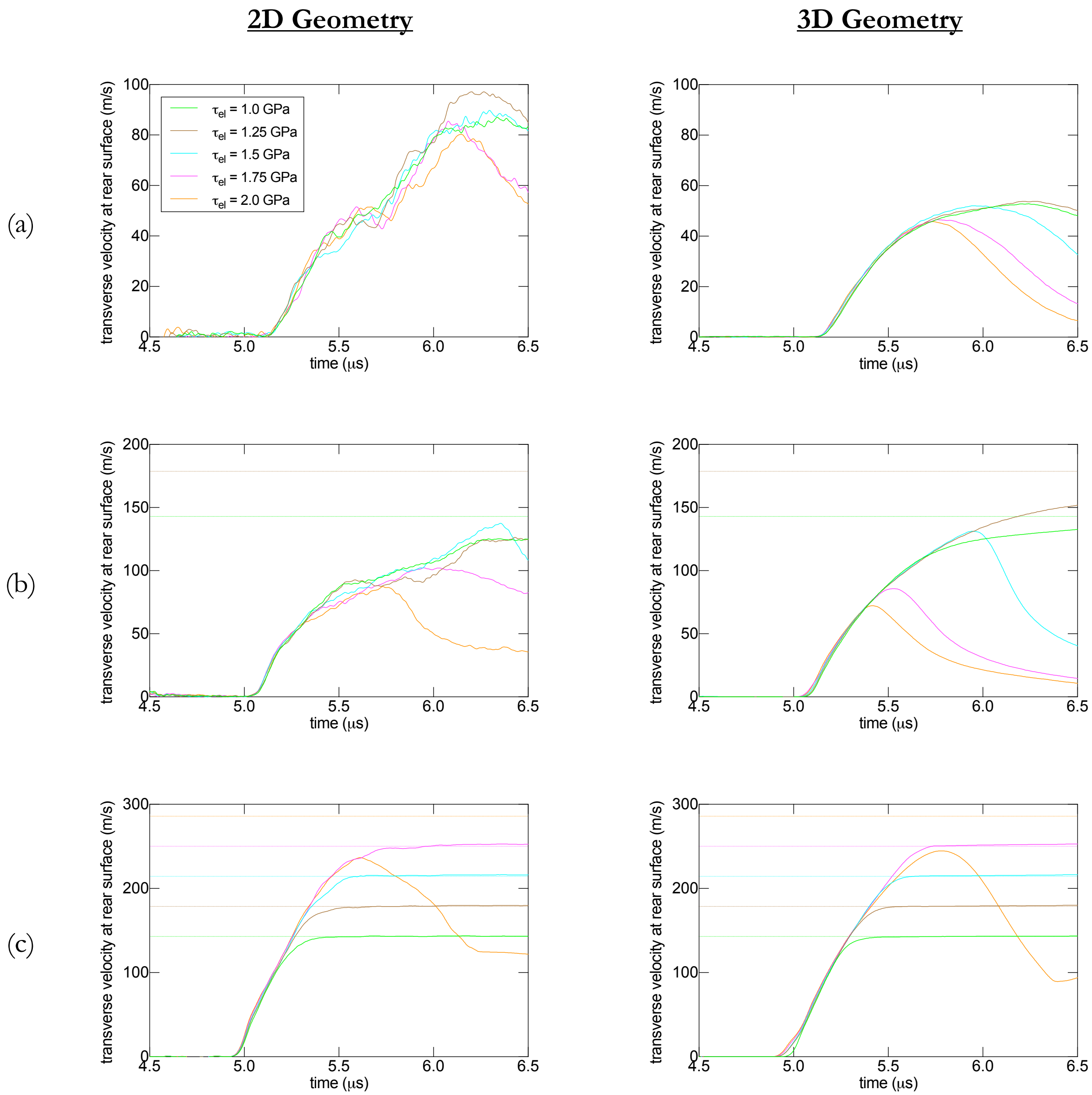

Figure 8. Transverse velocity history from 2D and 3D slide simulations at normal wave amplitudes σ_{el} of (a) 0.838, (b) 1.842, and (c) 4 GPa. For each value of σ_{el}, results are plotted for different shear wave amplitudes τ_{el} in the range of 1-2 GPa.

Transverse velocity histories from the rear target surface from simulations at the three σ_{el} values are shown in Figure 8. Results obtained for the 2D geometry are shown in the plots on the left, while results for the 3D geometry are shown in the plots on the right. For a given value of σ_{el}, both 2D and 3D simulations exhibit a clear upper bound in the transverse velocity. Moreover, the upper bounds increase with increasing σ_{el}. There is much more scatter in the transverse velocity histories near the upper bounds for the 2D simulations than for the 3D simulations, where the individual velocity histories form smooth upper bounds. This difference is due to the fewer number of grains (=332) in the 2D mesoscale powder model compared to the 3D model, which contains about 8× as many grains (=2483). For σ_{el} = 0.838 and 1.842 GPa, the upper bounds on the transverse velocities in both 2D and 3D simulations generally increase in time. However, for curves corresponding to the largest shear wave amplitudes τ_{el}, the transverse velocity histories exhibit a maximum followed by a decrease, as was observed in the 2D slide simulations discussed in the preceding paragraph. Such behavior indicates the formation of an internal shear interface in the sample and is found to be common to both 2D and 3D geometries. For 3D simulations, the time needed to form the internal shear interface decreases as τ_{el} is increased, which in turn leads to a decrease in the maximum transverse velocity. This is not always the case for the 2D simulations due to the large amount of scatter observed among the different runs. Comparing transverse velocity histories for the 2D and 3D geometries at σ_{el} = 0.838 GPa, the strain-hardening behavior appears to be more pronounced for the 2D geometry with the transverse velocity upper bound rising to near 100 m/s, while the upper bound for the 3D geometry does not exceed 55 m/s. At σ_{el} = 1.842 GPa, the trend seems to be the opposite with the transverse velocity upper bound in the 3D simulations reaching more than 150 m/s, while the upper bound for the 2D simulations remains below 140 m/s.

At σ_{el} = 4 GPa, the porosity is almost fully compressed out of the sample prior to the arrival of the shear wave. The nearly completely compacted sample can support much higher transverse velocities compared to the samples subject to lower confinement stress, which still retain a relatively high amount of porosity after being loaded by the normal wave. For simulations with $\tau_{el} < 2$ GPa, the transverse velocities after rise reach the expected transverse velocity levels, which are denoted by the horizontal dotted lines in Figure 8. However, at τ_{el} = 2 GPa, the simulated transverse velocity histories do not reach the expected transverse velocity level and, instead, exhibit a maximum followed by a large drop indicating formation of an internal shear interface in the sample. The transition from fully supporting the shear wave to formation of an internal shear interface is very sharp in this case, whereas at lower confinement stress the transition is more gradual and marked by a clear upper bound in the transverse velocity.

3.3. Effect of WC fracture strength on the dynamic shear strength

The simulations presented so far use a very simple model for tensile fracture of the WC grains that works by capping the tensile pressure (hydrostatic stress) in any cell containing WC material. If the tensile pressure in the cell reaches or exceeds the cap, void is introduced to raise the pressure of each material to the relaxation pressure, which is a function of the timestep, cell dimensions, and material volume fraction. No obvious fracturing of the grains is visible in the mesoscale powder model during pressure-shear loading at the shear failure surface. Therefore, to determine how much WC is near the fracture criterion, the stress tensor for cells containing non-zero volume fraction of WC is periodically output to file[*] and post-processed to calculate the mass fraction of WC that has tensile pressure ≥95% of the fracture stress σ_f, which is currently set to 4 GPa. Figure 9(a) shows the history of this quantity for a 2D simulation at an impact velocity of 189 m/s and skew angle of 70.9°, which corresponds to σ_{el} = 0.838 GPa and τ_{el} = 1.25 GPa. These impact conditions result in the mesoscale powder model being loaded to the shear failure surface, see Sec. 3.2. During the normal wave loading, very little grain material (<0.006%) reaches tensile pressures ≥95% σ_f. At the onset of shear loading, the fraction increases sharply but remains <0.016%. Calculations for the 3D geometry exhibit similar behavior, though the mass fractions of WC material ≥95% σ_f before and after the shear wave arrival are ~5× smaller. Thus, grain fracture is not a dominant failure mechanism in the simulations presented so far and the observed macroscopic shear flow is due almost exclusively to relative movement and deformation of grains.

---

[*] Requires updating to CTH version 12.2 to allow for proper filtering of cell data.

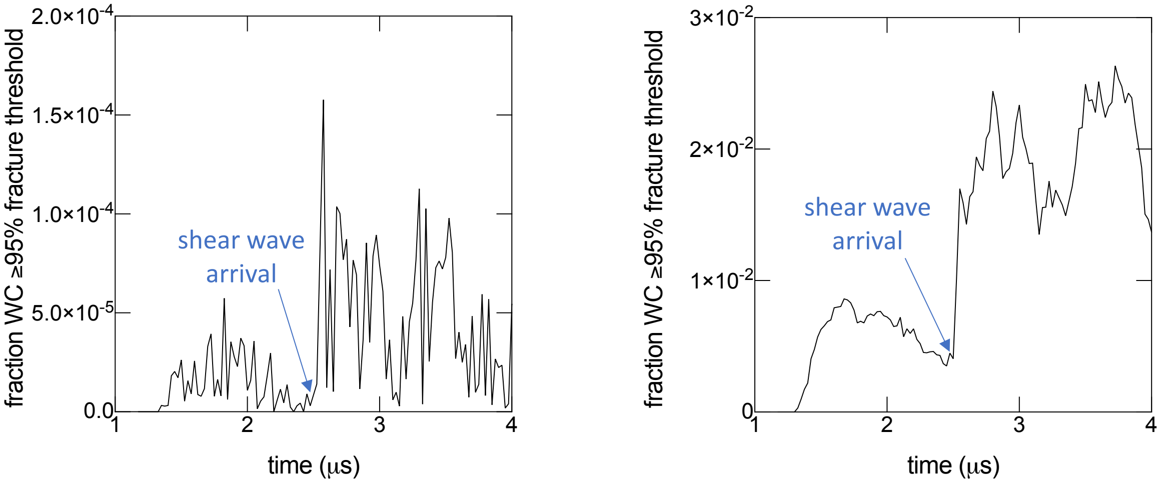

Figure 9. Plots showing the mass fraction of WC material ≥95% of the fracture stress given a fracture criterion based on tensile pressure (left) and maximum principal stress (right).

In CTH, it is possible to use the maximum principal stress as the fracture criterion instead of tensile pressure, which is the default. Given the same fracture stress, all stress states that lead to fracture for a fracture criterion based on tensile pressure will also lead to fracture for a fracture criterion based on maximum principal stress. The reverse is not true, so there exist stress states for which a fracture criterion based on maximum principal stress is satisfied, while one based on tensile pressure is not. To illustrate this, the same simulation data in the previous paragraph is used to calculate the fraction of WC with a maximum principal stress ≥95% σ_f. Results as a function of time are plotted in Figure 9(b) for the 2D geometry. Prior to the shear wave arrival, the peak mass fraction of WC material with a maximum principal stress ≥95% σ_f is ~0.85% and, after the shear wave arrival, the fraction jumps to >2%. Similar fractions are observed for calculations performed using the 3D geometry. Such values correspond to >100× more WC material than calculated for a fracture criterion based on tensile pressure.

Previous mesoscale simulations of single compaction shocks in granular WC varied the fracture stress from ~0 to 20 GPa with a baseline value of 4 GPa [28]. Results of these simulations showed little change in the bulk Hugoniot for fracture stresses above 2 GPa. However, for fracture stresses below 2 GPa, the bulk stiffness of the granular material was reduced until the limit of zero fracture stress, where a snowplow effect was observed in which any finite amplitude shock resulted in complete compaction of the sample to the Hugoniot for fully consolidated WC. The goal of the remainder of this section is to do a similar sweep of fracture stress for the WC grain material to determine what effect, if any, there is on the pressure-shear response of the mesoscale powder model. Fracture stresses $\sigma_f = 0, 0.1, 0.25, 0.5, 1, 2, 4, 8,$ and 20 GPa are chosen, which cover the same range as in previous mesoscale simulations. The CTH code requires $\sigma_f > 0$, so a small value of 1 Pa (10^{-9} GPa) is used to approximate material with zero fracture stress. For a given value of σ_f, simulation runs are performed fixing σ_{el} and varying the shear wave amplitude τ_{el} to determine the upper bound in transverse velocity that can be transmitted through the mesoscale powder model, as was done in Sec. 3.2. A fracture criterion based on maximum principal stress is used rather than one based on tensile pressure, which should result in more of the WC grain material reaching the fracture criterion, as discussed in the previous paragraph. Simulations are carried out for both the 2D and 3D geometries.

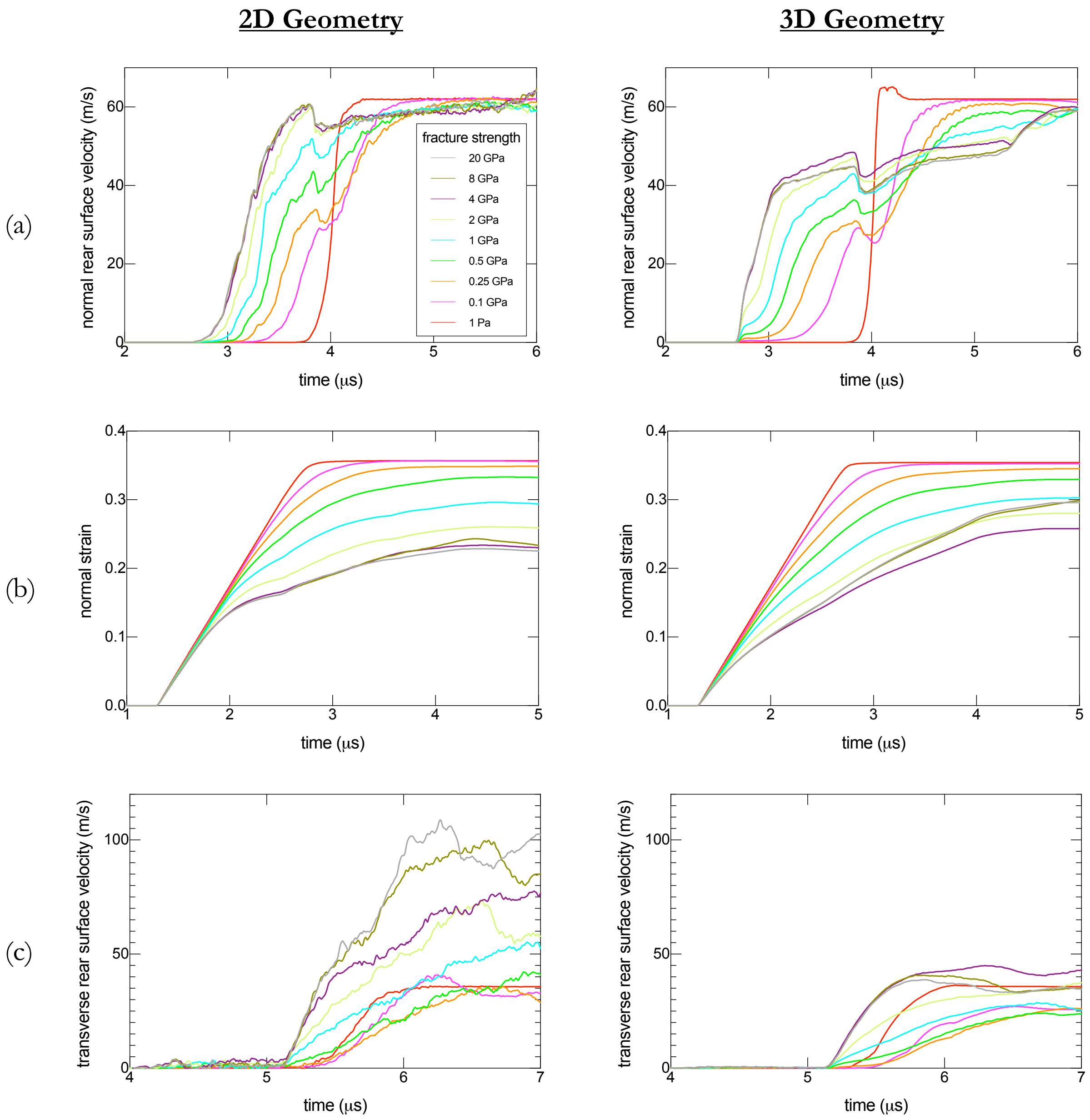

Figure 10. (a) Normal rear surface velocity histories, (b) normal strain histories, and (c) transverse rear surface velocity histories for mesoscale simulations with different fracture stresses for the WC grains at a stress confinement of 0.838 GPa. Each curve corresponds to the upper bound for several simulation runs performed with shear wave amplitudes τ_{el} = 0.25-2 GPa.

Normal and transverse rear surface velocity and normal strain histories for 2D and 3D mesoscale simulations with $\sigma_{el} = 0.838$ GPa are plotted in Figure 10. Each curve represents a different value for the WC fracture stress parameter σ_f and is determined by taking the upper bound in the simulation data for several runs varying τ_{el} over the range of 0.25-2 GPa. Looking at the normal velocity histories, we see that as σ_f is increased above the baseline value of 4 GPa, there is almost no change in the arrival time of the normal wave, indicating that the normal wave speed through the sample is unchanged. However, as σ_f is decreased below 4 GPa, the arrival of the normal wave becomes delayed, which indicates a decrease in the normal wave speed through the sample. In addition to the arrival time, the fracture stress also affects the normal wave rise. As σ_f is lowered below the baseline value, the height of the first shoulder in the normal velocity history decreases resulting in more compaction of the mesoscale powder model, which is clearly reflected in the normal strain history. In the limit of $\sigma_f = 0$ (1 Pa), a snowplow-like compaction response is observed in which the sample becomes fully compacted behind the normal wave front. This results in the slowest normal wave speed through the sample. Similar behavior of decreasing wave speed with decreasing fracture stress was observed in mesoscale simulations of normal compaction shocks in granular WC [28].

Looking at the transverse velocity histories, we see that the arrival time of the shear wave at the rear target surface is more or less the same as σ_f is lowered from 20 to 0.5 GPa. The major difference is that the transverse velocity rise becomes less steep with decreasing fracture stress. For $\sigma_f < 0.5$ GPa, there does appear to be some small delay in the arrival time of the shear wave, but the delay reaches a maximum for $\sigma_f = 0.1$ GPa and decreases slightly for the zero-fracture-stress case ($\sigma_f = 1$ Pa). In general, the trend is for the upper bound in the transverse velocity to decrease upon lowering the fracture stress of the WC grains. However, there is no significant change (beyond random noise) in the transverse velocity history upon decreasing σ_f from 20 to 8 GPa. At the other end of the spectrum, decreasing σ_f below 0.5 GPa does not result in any further reduction in the transverse velocity upper bound. Instead, the transverse velocity actually starts to steepen with decreasing fracture stress below 0.25 GPa. About 1 μs after the start of the shear wave rise, the transverse velocities for the 2D and 3D simulations with $\sigma_f = 0.5$ GPa are ~28 m/s and ~18 m/s, respectively. As a comparison, the simulations in Sec. 3.2, which used a tensile-pressure-based fracture criterion with $\sigma_f = 4$ GPa, give ~95 m/s and ~52 m/s over the same duration for the 2D and 3D simulations, respectively. In the experiment at the same stress confinement, the measured transverse velocity 1 μs after the start of the shear wave rise is ~14 m/s.

For the zero-fracture-strength case, the transverse velocity histories for both 2D and 3D simulations show a steady rise followed by a nearly constant plateau. Remember that a single curve in the plot corresponds to the upper bound in transverse velocity for several runs with different shear wave amplitudes. Plotting all runs separately would result in a set of curves similar to those in Figure 8(c) except that the transverse velocity magnitudes would be much less. This is because the simulations used to create the plots in that figure had a higher stress confinement, a tensile-pressure-based fracture criterion, and a higher fracture stress for WC. As was discussed in Sec. 3.2, such a set of curves indicates that the sample exhibits a sharp transition between fully supporting the amplitude of the shear wave to developing an internal shear interface. This same behavior is occurring for the current set of simulations at a lower stress confinement and with $\sigma_f = 0$ except that the sample cannot support as high shear wave amplitudes as the simulations presented in Sec. 3.2.

The same set of simulations sweeping σ_f over the range of 0-20 GPa is also performed at higher stress confinement $\sigma_{el} = 1.842$ GPa. Only simulations using the 2D geometry are carried out, as the 3D geometry had too high of a computational cost given the large number of runs needed. Normal and transverse velocity histories for the rear target surface for each value of σ_f are plotted in Figure 11, where again each curve corresponds to the upper bound from several simulation runs varying τ_{el} over the range of 0.25-2 GPa. As was found for $\sigma_{el} = 0.838$ GPa, decreasing σ_f leads to a delay in the normal wave arrival and, thus, a decrease in the normal shock speed through the sample. However, relative changes in the normal shock speed are smaller than those observed for the lower stress confinement, which is in agreement with results of previous mesoscale simulations [28]. There is some lowering of the initial shoulder in the normal velocity history with decreasing σ_f, but the effect is not as large as observed for $\sigma_{el} = 0.838$ GPa. Looking at the transverse velocity histories, we again see a decrease in the steepness of the shear wave rise and maximum transverse velocity with decreasing σ_f. However, the envelope containing all curves over the range of fracture stresses is smaller than observed for the lower stress confinement. The shear wave rise starts to steepen again for $\sigma_f < 1$ GPa and, for $\sigma_f \leq 0.1$ GPa, the transverse velocity exhibits a steady rise followed by a plateau. The minimum of the transverse velocity history curves occurs for $\sigma_f = 1$ GPa. About 1 μs after the start of the shear wave rise, the upper bound in transverse velocity is ~92 m/s for $\sigma_f = 1$ GPa. In comparison, the baseline simulations presented in Sec. 3.2 give an upper bound of ~109 m/s for the same duration after the shear wave rise, whereas the measured transverse velocity in experiment at the same stress confinement is ~34 m/s.

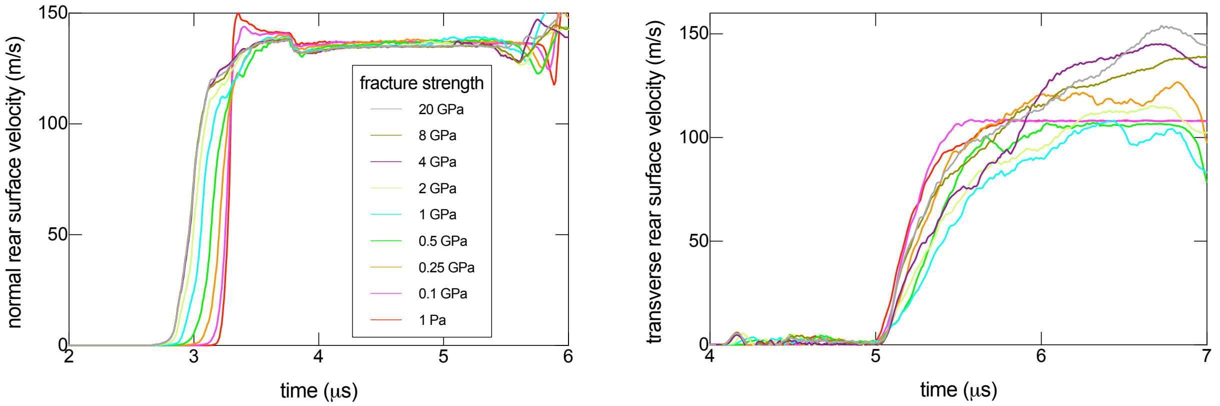

(a) (b)

Figure 11. (a) Normal and (b) transverse rear surface velocity histories for 2D mesoscale simulations with different fracture stresses for the WC grains at a stress confinement of 1.842 GPa. Each curve corresponds to the upper bound for several simulation runs performed with shear wave amplitudes τ_{el} = 0.25-2 GPa.

The mass fractions of WC grain material residing in cells where the maximum principal stress is ≥95% σ_f are plotted in Figure 12 for 2D simulations at $\sigma_{el} = 0.838$ and 1.842 GPa. The time window of the plot encompasses both the normal and shear wave loading. Results are shown for $\sigma_f = 0.5$ and 1 GPa for $\sigma_{el} = 0.838$ and 1.842 GPa, respectively. The choices for σ_f were motivated by the fact that these are the values at which the transverse velocity histories are at a minimum, see Figure 10(c) and Figure 11(b). The shear wave amplitude $\tau_{el} = 1$ GPa, which is high enough to cause the simulated sample to fail under shear at both levels of stress confinement. The first rise in the plots around 1 μs signals the arrival of the normal wave at the sample, while the spike around 2.5 μs signals the arrival of the shear wave. In both cases, the mass fraction of WC near the fracture criterion increases rapidly as the normal wave loads the sample. For $\sigma_{el} = 0.838$ GPa, the fraction continues to rise gradually until the arrival of the shear wave. In comparison, for $\sigma_{el} = 1.842$ GPa, the curve flattens out then decreases until the arrival of the shear wave. The shear wave arrival coincides with a spike in both curves, but the maximum is roughly 3× higher at the lower stress confinement. After the spike, the curves decrease on average for the remainder of the time window shown in the plot.

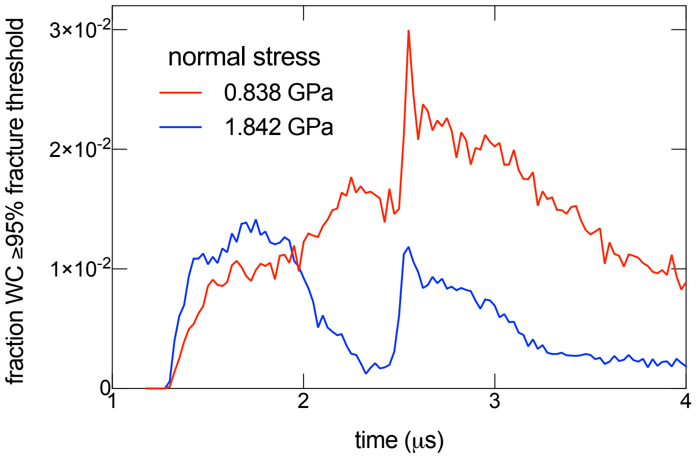

Figure 12. Plot showing the mass fraction of WC material ≥95% of the fracture stress for simulations at the shear failure surface for two different stress confinements.

4. DISCUSSION

Based on the results presented in Sec. 3.1, it is clear that the pressure-shear simulations using models and baseline parameter sets taken from previous mesoscale shock simulations on granular WC do not predict macroscopic shear failure at the conditions where shear failure is observed in experiment. However, by systematically increasing the amplitude of the shear wave, while keeping the amplitude of the normal wave fixed, simulations clearly show an upper bound in the transverse velocity recorded at the rear target surface. This upper bound was shown to be strongly dependent on the treatment of mixed-material cells within the sample. Enforcing stiction behavior at grain interfaces, which is the default treatment in multi-material hydrocodes, was shown to lead to a very high transverse velocity upper bound that is many times greater than observed in experiment for the same stress confinement. However, when sliding of grains was enforced, the upper bound in transverse velocity was shown to be substantially smaller. For simulations at low stress confinement, in which the sample retains significant porosity after being loaded by the normal wave, the upper bound in transverse velocity was found to increase over time, see Figure 8(a) and (b), indicating significant strain-hardening behavior. By contrast, the transverse velocities measured in experiment reach a fairly steady state after ~0.2-0.6 μs from the start of the shear wave rise with comparatively modest increases, see Figure 5(a).

The strain-hardening behavior observed in the simulations arises from grains rearranging themselves to form more stable configurations, which allows for transmission of higher transverse velocities through the sample over time. The rearrangement continues until the release wave arrives from the rear surface of the target or, for simulations with sliding among grains, an internal shear interface forms within the sample that spans the entire transverse dimension. Once the internal shear interface forms, transverse velocities can no longer be transmitted as effectively through the sample, which results in a drop in the transverse velocity recorded at the rear surface. Exceptions to the strain-hardening behavior were observed for simulations presented in Sec. 3.2 for the highest stress confinement of 4 GPa as well as for some of the simulations using low fracture stresses for the WC grains presented in Sec. 3.3. In these cases, almost all porosity was compressed out of the mesoscale powder model prior to loading by the shear wave, so no significant grain rearrangement could occur to increase the flow strength of the sample. Instead, the sample either fully supported the shear wave amplitude, resulting in a constant transverse velocity after rise, or an internal shear interface formed within the sample, resulting in a rise then sudden drop.

Post-shot recovery SEM images of the granular samples in experiment showed significant comminution as a result of the shear loading. Initial samples had a grain size distribution of 20-32 μm, while recovered particles were mostly 2-3 μm with many <1 μm [16]. For the slide simulations presented in Sec. 3.1, localized regions appeared in the sample where grains were observed to break up and flow. The flow regions were found to be exacerbated at low stress confinement. Significant break up and flow of grains was also observed on either side of an internal shear interface for the simulations at the shear failure surface that were presented in Sec. 3.2. However, the grains that were broken up were limited to areas in direct contact with the shear interface, while grains in the remainder of the sample were largely unaffected. In both contexts, the flow was more significant in the 3D simulations than in 2D simulations. For the simulations presented in Sec. 3.1 and 3.2, a fracture criterion based on tensile pressure was used for the WC grains with a fracture stress of 4 GPa taken from previous mesoscale simulation work. Statistical calculations of the stress state for cells containing WC revealed that almost none of the grain material was getting close to the fracture criterion even when the sample was loaded to the shear failure surface. In light of this finding, the localized flow regions and areas on either side of an internal shear interface that show breaking up and flowing of grains are most likely an artifact of the slide algorithm and not due to fracturing of grains.

In Sec. 3.3, it was shown that an alternate fracture criterion based on the maximum principal stress component led to much more of the WC grain material getting close to the fracture criterion than when the default fracture criterion based on tensile pressure was used. Although not shown explicitly, this alternate fracture criterion led to a reduction in the transverse velocity that could be supported by the mesoscale powder model. By switching to the principal-stress-based fracture criterion and lowering the fracture stress of the WC grain material from its baseline value of 4 GPa to 0.5 GPa while keeping all other simulation settings the same, it was found that the upper bound in transverse velocity could be reduced even further. At a stress confinement of 0.838 GPa, the upper bound in the transverse velocity was reduced by ~70% for both 2D and 3D simulations, thus bringing the simulation results more in line with experiment. The baseline fracture stress for WC of 4 GPa was motivated by spall strength measurements of hot-pressed WC [35]. As a comparison, the ultimate tensile strength of WC under quasi-static loading conditions is 0.59 GPa [36]. The loading conditions for tensile tests may be more representative of those occurring in individual grains within a partially compacted powder during pressure-shear loading than those under which spall strength measurements are performed on solid WC. Therefore, a fracture stress of 0.5 GPa for the simulated WC grains is not unreasonable.

At the higher stress confinement of 1.842 GPa, it was shown that varying the fracture stress of the WC grains did not produce as much of an effect on the shear strength of the simulated powder as observed for the lower stress confinement of 0.838 GPa. Moreover, it was shown that the simulations diverged from the experimental shear response with the simulated powders exhibiting higher shear strengths with increasing stress confinement. Although only confirmed for the 2D simulations, the same trend is thought to occur in the 3D simulations as well. At the end of Sec. 3.3, it was shown that there was a lower fraction of WC near the fracture criterion during shear loading at the higher confinement stress despite similar fractions during loading by the normal wave. As the confinement stress is increased, the powder is compacted more (lower porosity) before being loaded by the shear wave. Clearly, there are fewer stress states near the fracture criterion for more compacted powders, which results in the fracture stress having less of an effect on the shear response than observed for less compacted powders. In the simulations, fracture is treated by inserting void into a cell that has reached the fracture criterion. Afterwards, void can be compressed out and the material retains no record of the fracture having occurred. This is not representative of how the powder behaves in experiment, where fractured grains remain as distinct material pieces despite further compression.

5. CONCLUSIONS

In this work, Eulerian simulations of pressure-shear loading were presented for a granular ceramic material described by a simple mesoscale model composed of a random arrangement of solid circular or spherical grains. Material models and baseline parameter sets for WC were taken from previous mesoscale simulations of normal shocks in WC powder [27]. Results of 2D and 3D simulations with either stiction or sliding behavior for the grains were compared directly to pressure-shear experiments on dry granular WC [16]. In general, simulations exhibit a more rapid rise to the normal stress state than observed in experiment with the 3D slide simulations exhibiting the best overall agreement, though still being overly stiff during the initial part of the normal wave rise prior to reverberations. Furthermore, simulated samples did not exhibit signs of macroscopic shear failure at the same conditions as in experiment. Stiction simulations showed transverse velocities after rise at the amplitude of the initial shear wave for all experimental impact conditions indicating the sample was responding elastically to the shear wave. Slide simulations did exhibit transverse velocities below the shear wave amplitude. However, the reduction in the transmitted transverse velocity was attributed to localized flow regions at grain interfaces and not due to macroscopic shear flow. These localized flow regions, which were more pronounced in 3D than 2D and exacerbated at low impact velocities, are believed to be nonphysical and most likely a byproduct of the slide algorithm.

To probe the shear failure surface of the mesoscale powder model, simulations were carried out for a range of shear wave amplitudes, far exceeding the range possible in experiment. Simulated transverse velocities were found to be bounded with respect to increasing shear wave amplitude, thus providing a measure of the shear failure surface for the simulated powders. The dynamic shear strength was found to depend strongly on the approximate grain interface treatment and, to a much smaller degree, on the number of dimensions. Simulations with sliding grains exhibited much lower shear strengths than simulations with the default grain stiction behavior. In addition, higher stress confinement was shown to lead to higher shear strength, which is in agreement with experiment. The fracture stress of the grains was also shown to affect the macroscopic shear failure response with lower fracture stresses yielding lower shear strengths, but with a lower limit beyond which decreasing the fracture stress did not lead to any further reduction in strength. Lowering the fracture stress of the grains also increased the compaction of the simulated powders making the results more in line with experimental observations. At partial compactions, simulations exhibited strain-hardening behavior initially followed, in most cases, by a drop in the flow stress resulting from formation of an internal shear interface within the sample. Near full compaction, there was no strain-hardening behavior. Instead, a sharp transition was observed between the sample being able to support the full amplitude of the shear wave to formation of an internal shear interface after which the sample retained little to no shear strength. By contrast, experiments exhibited a fairly steady transverse velocity level after rise with little or no strain-hardening behavior.

By including an approximate treatment of sliding interfaces and treating the fracture stress as a variable parameter, results of the mesoscale simulations started to approach results of pressure-shear experiments on granular WC at low stress confinement (~1 GPa). However, agreement with experiment was found to worsen with increasing confinement stress as simulations more severely overpredict the dynamic shear strength. The mesoscale simulations suffer from numerical issues arising from the approximate treatment of sliding grain interfaces, such as localized flow regions at low impact velocities that manifest at grain interfaces and formation of internal shear interfaces that span the cross-section of the simulation domain. Moreover, fracture of the grains is not treated realistically in the simulations, which can lead to fractured grains healing upon recompression.

Ultimately, both of these issues stem from the Eulerian nature of the simulations, which does not resolve interfaces between grains explicitly, so the simulations are forced to rely on ad hoc methods to treat contact and fracture. Future work should look into other methods, like Lagrangian finite element simulations, which use body-fitted meshes and can handle contact explicitly, or peridynamics, which as an integral continuum mechanics formulation that is better suited to handle cracks and discontinuities.

REFERENCES

[1] P. Lambert and H Trumel, in *Materials under Extreme Loadings: Applications to Penetration and Impact*, edited by G. Voyiadjis, E. Buzaud and I. R. Ionescu (Wiley, 2010).

[2] M. Iskander, S. Bless and M. Omidvar, *Rapid Penetration into Granular Media : Visualizing the Fundamental Physics of Rapid Earth Penetration*, (Elsevier, 2015).

[3] W.A. Gooch, *An overview of ceramic armor applications,* Ceramic Transactions **134** , 3-21 (2002).

[4] D. A. Shockey, A. H. Marchand, S. R. Skaggs, G. E. Cort, M. W. Burkett and R. Parker, *Failure phenomenology of confined ceramic targets and impacting rods*, International Journal of Impact Engineering **9** (3), 263-275 (1990).

[5] M. A. Meyers, *Dynamic Behavior of Materials.* (Wiley, 1994).

[6] T. Akashi, V. Lotrich, A. Sawaoka and E. K. Beauchamp, *Shock consolidation of coarse SiC powder*, Journal of the American Ceramic Society **68** (12), 322-324 (1985).

[7] K.I. Kondo, S. Soga, A. Sawaoka and M. Araki, *Shock compaction of silicon carbide powder*, Journal of Materials Science **20** (3), 1033-1048 (1985).

[8] T. Taniguchi, K. Kondo and A. Sawaoka, *Shock compression of powder compacts of* CaF_2, Journal of Applied Physics **61** (1), 196-200 (1987).

[9] J.A. Akins and T.J. Ahrens, *Dynamic compression of* SiO_2*: A new interpretation*, Geophysical Research Letters **29** (10), 31-31-31-34 (2002).

[10] J. P. Borg, D. J. Chapman, K. Tsembelis, W. G. Proud and J. R. Cogar, *Dynamic compaction of porous silica powder*, Journal of Applied Physics **98** (7), 073509 (2005).

[11] J. L. Brown, T. J. Vogler, D. E. Grady, W. D. Reinhart, L. C. Chhabildas and T. F. Thornhill, *Dynamic compaction of sand*, AIP Conference Proceedings **955** (1), 1363-1366 (2007).

[12] W. G. Proud, D. J. Chapman, D. M. Williamson, K. Tsembelis, J. Addiss, A. Bragov, A. Lomunov, I. G. Cullis, P. D. Church, P. Gould, D. Porter, J. R. Cogar and J. Borg, *The dynamic compaction of sand and related porous systems*, AIP Conference Proceedings **955** (1), 1403-1408 (2007).

[13] T. J. Vogler, M. Y. Lee and D. E. Grady, *Static and dynamic compaction of ceramic powders*, International Journal of Solids and Structures **44** (2), 636-658 (2007).

[14] A. S. Abou-Sayed, R. J. Clifton and L. Hermann, *The oblique-plate impact experiment*, Experimental Mechanics **16** (4), 127-132 (1976).

[15] J. W. LaJeunesse, *Dynamic Behavior of Granular Earth Materials Subjected to Pressure-shear Loading*, Ph.D. thesis, Marquette University, 2018.

[16] W. D. Reinhart, T. F. Thornhill, III, T. J. Vogler and C. S. Alexander, *Pressure-shear experiments on granular materials*, Sandia National Laboratories Report No. SAND2011-6700, 2011 (unpublished).

[17] S. Sairam and R. J. Clifton, *Pressure-shear impact investigation of dynamic fragmentation and flow of ceramics*, Brown University Report No. AD-A-296109/2/XAB, 1994 (unpublished).

[18] X. Sun, A. Chauhan, D. D. Mallick, A. L. Tonge, J. W. McCauley, K. J. Hemker, J. C. LaSalvia and K. T. Ramesh, *Granular flow of an advanced ceramic under ultra-high strain rates and high pressures*, Journal of the Mechanics and Physics of Solids **143**, 104031 (2020).

[19] R. L. Williamson, *Parametric studies of dynamic powder consolidation using a particle-level numerical model*, Journal of Applied Physics **68** (3), 1287-1296 (1990).

[20] D. J. Benson, *An analysis by direct numerical simulation of the effects of particle morphology on the shock compaction of copper powder*, Modelling and Simulation in Materials Science and Engineering **2** (3A), 535 (1994).

[21] D. J. Benson and W. J. Nellis, *Dynamic compaction of copper powder: Computation and experiment*, Applied Physics Letters **65** (4), 418-420 (1994).

[22] D. J. Benson, V. F. Nesterenko, F. Jonsdottir and M. A. Meyers, *Quasistatic and dynamic regimes of granular material deformation under impulse loading*, Journal of the Mechanics and Physics of Solids **45** (11), 1955-1999 (1997).

[23] M. A. Meyers, D. J. Benson and E. A. Olevsky, *Shock consolidation: microstructurally-based analysis and computational modeling*, Acta Materialia **47** (7), 2089-2108 (1999).

[24] D. J. Benson, W. Tong and G. Ravichandran, *Particle-level modeling of dynamic consolidation of Ti-SiC powders*, Modelling and Simulation in Materials Science and Engineering **3** (6), 771 (1995).

[25] J. P. Borg and T. J. Vogler, *Mesoscale calculations of shock loaded granular ceramics*, AIP Conference Proceedings **955** (1), 227-230 (2007).

[26] T. J. Vogler and J. P. Borg, *Mesoscale and continuum calculations of wave profiles for shock-loaded granular ceramics*, AIP Conference Proceedings **955** (1), 291-294 (2007).

[27] J. P. Borg and T. J. Vogler, *Mesoscale calculations of the dynamic behavior of a granular ceramic*, International Journal of Solids and Structures **45** (6), 1676-1696 (2008).

[28] J. P. Borg and T. J. Vogler, *Aspects of simulating the dynamic compaction of a granular ceramic*, Modelling and Simulation in Materials Science and Engineering **17** (4), 045003 (2009).

[29] J. P. Borg, T. J. Vogler and A. Fraser, *A review of mesoscale simulations of granular materials*, AIP Conference Proceedings **1195** (1), 1331-1336 (2009).

[30] J. P. Borg and T. J. Vogler, *Rapid compaction of granular material: characterizing two- and three-dimensional mesoscale simulations*, Shock Waves **23** (2), 153-176 (2013).

[31] J. M. McGlaun, S. L. Thompson and M. G. Elrick, *CTH: A three-dimensional shock wave physics code*, International Journal of Impact Engineering **10** (1), 351-360 (1990).

[32] S. Plimpton, *Fast Parallel Algorithms for Short-Range Molecular Dynamics*, Journal of Computational Physics **117** (1), 1-19 (1995).

[33] D. P. Dandekar and S. V. Spletzer, *Shock response of Ti-6Al-4V*, AIP Conference Proceedings **505** (1), 427-430 (2000).

[34] J. L. Finney and J. D. Bernal, *Random packings and the structure of simple liquids I. The geometry of random close packing*, Proceedings of the Royal Society of London. A. Mathematical and Physical Sciences **319** (1539), 479-493 (1970).

[35] D. P. Dandekar, *Spall Strength of Tungsten Carbide*, Army Research Laboratory Report No. ARL-TR-3335, 2004.

[36] W. A. Gooch, M. S. Burkins and R. Palicka, *Ballistic development of U.S. high density tungsten carbide ceramics*, J. Phys. IV France **10** (PR9), 741-746 (2000).

This page left blank

DISTRIBUTION

Email—Internal

Name	Org.	Sandia Email Address
Scott Alexander	01647	calexa@sandia.gov
Chris Johnson	01647	cjohns6@sandia.gov
Jeff LaJeunesse	05417	jwlajeu@sandia.gov
Seth Root	05912	sroot@sandia.gov
Shane Schumacher	01555	scschum@sandia.gov
Russell Teeter	01555	rdteete@sandia.gov
Tracy Vogler	08363	tjvogle@sandia.gov
Travis Voorhees	08363	tjvoorh@sandia.gov
Technical Library	01977	sanddocs@sandia.gov

Sandia National Laboratories